Field Reconstruction Method for Linear Tubular Permanent Magnet Motor

KI-HOON KIM [ID], (Student Member, IEEE), AND DONG-KYUN WOO [ID]
Department of Electrical Engineering, Yeungnam University, Gyeongsan 38541, South Korea

Corresponding author: Dong-Kyun Woo (wdkyun@yu.ac.kr)

ABSTRACT This paper considers a linear tubular permanent magnet motor (LTPMM) for an active suspension system. The LTPMM has an end effect due to its structure. This can be an important factor for analysis and design of the LTPMM because it distorts the air-gap magnetic flux distribution. The field reconstruction method (FRM) was developed for an effective evaluation of the magnetic field in the electric machine. It can reduce the computation time using the basis-function which reconstructs the air-gap magnetic flux distribution with a static finite element analysis. In this paper, we adopted the FRM to evaluate the LTPMM. However, the FRM has been applied only to the rotating machines and does not take into account the distortion of the magnetic flux distribution in the LTPMM. To deal with this problem, we proposed an enhanced FRM with new basis-function. The proposed method is verified by comparing between experiment result, conventional and enhanced FRM.

INDEX TERMS Active suspension system, linear active suspension, linear permanent magnet motor, field reconstruction method.

I. INTRODUCTION

In the automotive industry, the current and the future trend are becoming more electrified vehicles. The hybrid electric vehicle (HEV) combines an electric motor with a combustion engine in order to increase efficiency. In the electric vehicle (EV), the combustion engine has been replaced by an electric motor.

Recently, many studies have been conducted to improve the driving quality in HEV and EV [1], [2]. The active suspension system can improve performance without conflicting demands between road condition, load carrying, and passenger comfort [3]. Therefore, the traditional passive suspension system will gradually be replaced by the active suspension system in the near future.

For the active suspension system using the electric machine (EM), both rotating and linear machines can be applied. The linear machine is more efficient than the rotating machine because the electromagnetic energy can be directly transferred without conversion from rotational motion to linear motion.

The EMs are becoming increasingly diverse and require proper mathematical modeling. The accuracy of modeling is an important factor in analysis and design of the EM.

The magnetic equivalent circuit or the analytical method was widely used as an analysis tool offering a good compromise between accuracy and computational cost [4]. These methods could be applied to various types of EMs. However, it has a limitation in considering the detail structure inside the EM. For this problem, the finite element (FE) analysis is used.

The two-dimensional (2-D) FE analysis is much faster than the three-dimensional (3-D) FE analysis, however, it does not reflect the electromagnetic effects caused by the 3-D structure, making it difficult to guarantee accuracy when evaluating models with complex shapes. On the other hand, 3-D FE analysis is computationally inefficient for the optimal design process.

To address this problem, the field-based approach using the FE analysis can be used. The field reconstruction method (FRM) has been used to reduce the computational burden in the FE analysis [5]–[8]. In the FRM, the air-gap magnetic flux density is presented as the sum of each magnetic flux distribution generated from permanent magnet (PM) and armature winding. Each magnetic flux distribution is reconstructed by the basis-function sweeping the reference magnetic flux distribution. By using the basis-function, it is possible to calculate the air-gap magnetic flux distribution at the combination of any armature current or mover position without an additional FE analysis [7], [8].
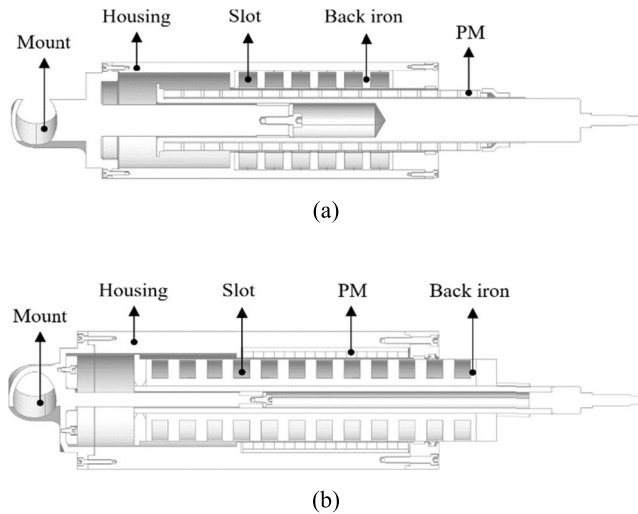
The associate editor coordinating the review of this manuscript and approving it for publication was Jenny Mahoney.

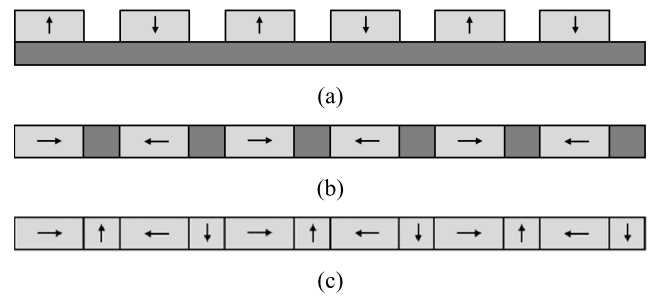FIGURE 1. LTPMM. (a) Interior PM type. (b) Exterior PM type.

FIGURE 2. Magnetization pattern. (a) Radial magnetization. (b) Axial magnetization. (c) Halbach magnetization.

TABLE 1. Basic specification of LTPMM.

Mover outer radius R_{mo} [mm]	45
Mover inner radius R_{mi} [mm]	39
Stator inner radius R_{si} [mm]	12.5
Slot length S_l [mm]	14
Slot depth S_d [mm]	18
Slot pitch τ_s [mm]	10
Magnet depth M_d [mm]	6
Stroke x [mm]	144
Air gap length l [mm]	288
Magnet length M_l [mm]	9
Air gap g [mm]	1.5

Therefore, the FRM can reduce the computational burden of the FE analysis.

The previous research work on the FRM has focused on the applications, such as axial flux PM motors [6]–[8], switched reluctance machines [9], PM synchronous machines [10]–[13], and induction machines [14], [15]. Park *et al*. [6] and Ajily *et al*. [7] presented the performance of axial flux PM motors using the 3-D FRM. Lin *et al*. [9] proposed a way to apply the FRM to a switched reluctance machine to consider the double-saliency and magnetic saturation. For efficient modeling, Torregrossa *et al*. [10], [11] and Dezheng *et al*. [14]. used the FRM for the synchronous PM motors and induction machines, respectively. However, few papers have reported the FRM in linear machines. The focus is always on rotating machines, not linear-type machines.

In this paper, we adopted FRM for the analysis and design of the LTPMM. The LTPMM is structurally accompanied by a longitudinal end effect, which distorts the magnetic flux distribution in the air-gap [16], [17]. This effect can be further increased because the electromagnetic active suspension has a shorter stroke. Therefore, accurate analysis of this effect is important for designing the LTPMM. First, we evaluated the distortion of air-gap magnetic flux distribution due to the longitudinal end effect of the LTPMM. Then, we proposed the enhanced FRM with a new basis-function.

II. ELECTROMAGNETIC ACTIVE SUSPENSION
A. LINEAR TUBULAR PERMANENT MAGNET MOTOR
The linear machine can be classified as the linear planner permanent magnet motor (LPPMM) and the linear tubular permanent magnet motor (LTPMM) [18], [19]. The LTPMM has an advantage that the force density is higher than that of the LPPMM because the attraction force is zero [20].

The LTPMM can be sorted into interior PM type and exterior PM type according to the relative position of the PM. Fig. 1 show the LTPMM with interior PM type and exterior PM type, respectively. Magnetization can be categorized into axial, radial and halbach pattern according to the direction of the magnetization as shown in Fig. 2.

In an electric machine with the halbach magnetized PM, the air-gap magnetic flux distribution and the back-EMF waveform are more sinusoidal and the detent force is low. In addition, the halbach array does not require the back-iron for the PM, resulting in higher power density than other magnetization patterns under the same volume condition [21], [22].

Because the active suspension system locates outside of the vehicle, it would be exposed to the external pollution such as dust and sand. Therefore, the interior PM type is weaker in the external environment than the exterior PM type. As a result, we adopted the LTPMM with exterior PM type and the halbach array. The specification of the analysis model and its structure are shown in Table 1 and in Fig. 3, respectively.

B. MAGNETIC FLUX DISTRIBUTION IN LTPMM
In this paper, the LTPMM includes coupled modules. A single module of the PM and stator consists of 4-poles and 3-slots, respectively. In Fig. 1 (b), since the LTPMM has 4-modules of the stator and 2-modules of the mover, the air-gap magnetic flux distribution is repeated every slot pitch.

For the electromagnetic active suspension, the LTPMM has a short mover and short stator due to spatial constraints. Because of the different lengths of the mover and stator, the LTPMM has a longitudinal end effect as shown in Fig. 4. The effect distorts the periodicity of the air-gap magnetic flux distribution, affecting the thrust force. This will result in unpredictable characteristics.

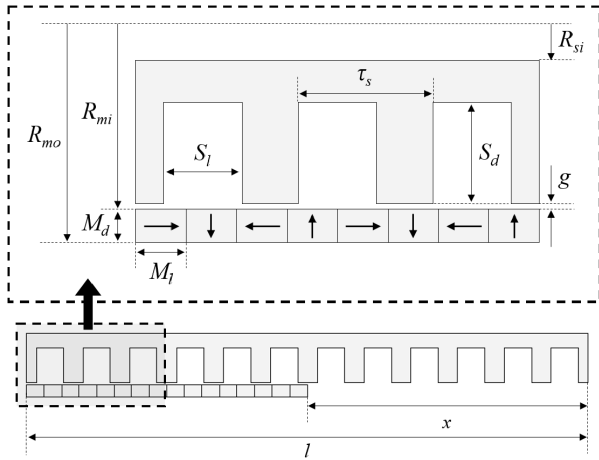Fig. 6 shows the *r*-component of the air-gap magnetic flux distribution under no-load conditions. The results were
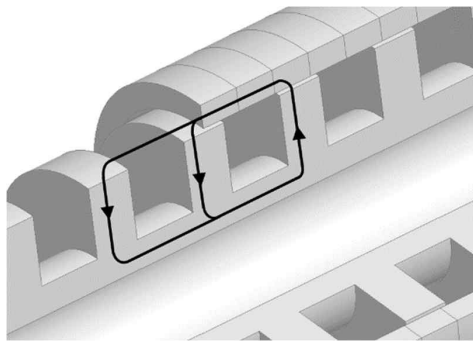
FIGURE 3. Design parameters.

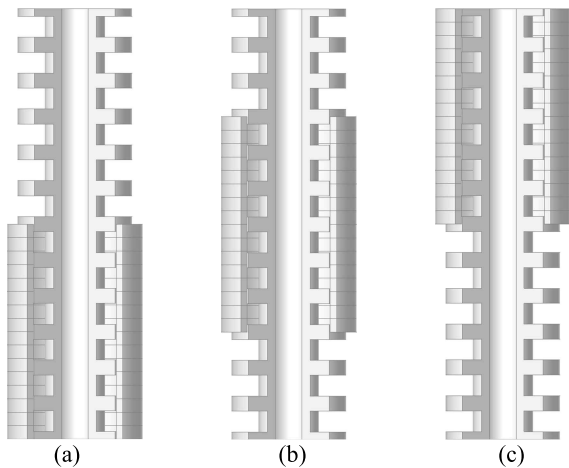**FIGURE 4.** Longitudinal end effect in LTPMM.

FIGURE 5. Initial position of mover. (a) Mover moved $0\tau_s$ from the left end of the stator. (b) Mover moved $3\tau_s$ from the left end of the stator. (c) Mover moved $6\tau_s$ from the left end of the stator.

obtained when the mover moved 0, $3\tau_s$, and $6\tau_s$ from the left end of the stator in Fig. 5. In Fig. 6 (b), the results represents the longitudinal end effect at both ends of the PM and τ_{end} is the distance affected by the longitudinal end effect. In Fig. 6 (a) and (b), however, when the PM reaches the end of the stator, the reluctance paths at both ends of the PM gradually change, eventually making the three waveforms different.
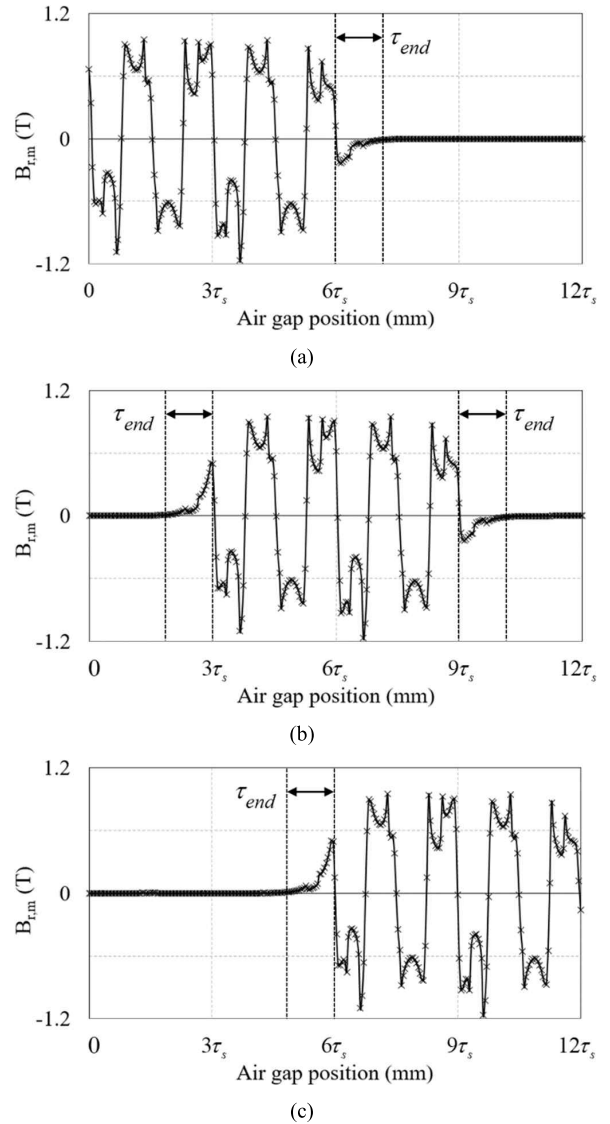
FIGURE 6. Radial component of air-gap magnetic flux distribution by PM. (a) Mover is located on the initial position. (b) Mover moved $3\tau_s$ from the left end of the stator. (c) Mover moved $6\tau_s$ from the left end of the stator.

III. CONVENTIONAL FRM

In the conventional FRM, an air-gap magnetic flux density is obtained as follows [23], [24]:

$$B_r(t) = B_{r,m}(t) + B_{r,s}(t) \tag{1}$$

$$B_z(t) = B_{z,m}(t) + B_{z,s}(t) \tag{2}$$

where $B_r(t)$ and $B_z(t)$ are the air-gap magnetic flux density in the r-, and z-direction in cylindrical coordinate system, and $B_m(t)$ and $B_s(t)$ are the air-gap magnetic flux density generated by PM and armature reaction, respectively.

The $B_m(t)$ and $B_s(t)$ are reconstructed by using the following basis-functions [6]:

$$B_m(t) = f_m(t) \tag{3}$$

$$B_s(t) = \sum_{a=1}^{N} B_{s,a}(t) \tag{4}$$

$$B_{s,a}(t) = f_s \cdot i_{s,a}(t) \tag{5}$$

where f_m and f_s are the basis-functions of the mover and the stator, $i_{s,a}(t)$ is the excitation current in the ath slot, $B_{s,a}(t)$ is the air-gap magnetic flux density when the ath slot is only excited, and N is the number of slots.

In order to reconstruct the entire air-gap magnetic flux density, the basis-function sweeps the reference magnetic flux distribution. The reference magnetic flux distribution is obtained by the FE static analysis. The basis-function predicts the distribution of the air-gap field over the entire position of the mover by sweeping.

The conventional FRM assumes that the air-gap magnetic flux distribution is periodic and the air-gap is continuous. Under this condition, the reference magnetic flux distribution can be selected at any mover position. Unlike a linear machine, the air-gap of a rotating machine has continuity that is repeated for every pole pitch.

However, in the case of the linear motor, the field distribution varies depending on the position of the mover as shown in Fig. 6. Therefore, when the FRM is applied to a rotating machine, the reference magnetic flux distribution can be selected at any position of the mover. However, in the case of the LTPMM with the finite air-gap length, the air-gap is not continuous and the air-gap magnetic flux is distributed without a periodicity.

In Fig. 6, the air-gap magnetic flux distributions in each case are different in τ_{end}. If one of three waveforms is selected as the reference magnetic flux distribution, the basis-function will sweep this difference at all mover positons. It will distort the overall air-gap magnetic flux density and eventually results in unexpected characteristics. Therefore, an accurate evaluation of the end effect is required in the FRM. For this reason, the conventional FRM should be modified in order to be applied to the LTPMM.

IV. ENHANCED FRM

A. BASIS FUNCTION: STATOR

In the proposed FRM, the air-gap magnetic flux density generated by the armature reaction is expressed as follows:

$$B_s(t) = F_s \cdot I_s(t) \tag{6}$$

$$I_s(t) = \begin{bmatrix} i_{s,1}(t + \theta_1) & i_{s,2}(t + \theta_2) & \cdots & i_{s,N}(t + \theta_N) \end{bmatrix}^T \tag{7}$$

$$F_s = \begin{bmatrix} f_s\left(L_{s,1}^1(t_0)\right) & f_s\left(L_{s,2}^1(t_0)\right) & \cdots & f_s\left(L_{s,N}^1(t_0)\right) \\ f_s\left(L_{s,1}^2(t_0)\right) & f_s\left(L_{s,2}^2(t_0)\right) & \cdots & f_s\left(L_{s,N}^2(t_0)\right) \\ \vdots & \vdots & \ddots & \vdots \\ f_s\left(L_{s,1}^k(t_0)\right) & f_s\left(L_{s,2}^k(t_0)\right) & \cdots & f_s\left(L_{s,N}^k(t_0)\right) \end{bmatrix} \tag{8}$$

where f_s is the basis-function of the stator, F_s is the basis-matrix of the stator, θ_N is the phase angle of Nth slot, t_0 is the initial time, and $L_{s,N}^k$ represents the reference magnetic flux distribution. It can be obtained as follows:

$$L_{s,N}^k(t_0) = \frac{B_{s,N}(t_0, I_0)}{I_0} \tag{9}$$
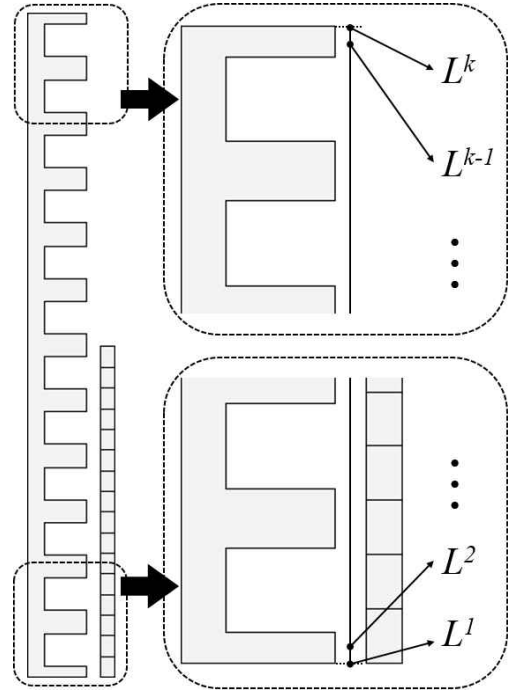

FIGURE 7. Position of the reference magnetic flux distribution in air-gap.

where I_0 is the initial current. As shown in Fig. 7, $L_{s,N}^k$ is the magnetic flux density at kth position in the air-gap. It is generated by the armature reaction in Nth slot.

In this paper, because the LTPMM adopted the halbach magnetization, the back-iron of the mover is not needed. In addition, since the stator has the same length as the air-gap, there is no distortion of the magnetic flux distribution due to the longitudinal end effect when the armature winding is excited and the PM is excluded. Therefore, for the basis-function of the stator f_s, $B_{s,N}$ requires only a static FE analysis.

Fig. 8 shows the results of the conventional FRM, enhanced FRM, and finite element method (FEM). Fig. 8 presents the r- and z-component of the air-gap flux distribution at the left end of the PM. Using the FEM, the air-gap flux density was obtained when the mover moved $3\tau_s$ from the initial position. The results of the FRMs were generated by sweeping the reference magnetic flux distribution at initial position. The difference between the results of the FRM and FEM is acceptable below 2.8%.

B. BASIS FUNCTION: MOVER

First, as shown in Fig. 6 (b), when the mover is located more than τ_{end} from the end of the stator, the air-gap magnetic flux density can be obtained as follows:

$$B_m(t) = \sum_{h=1}^{P} F_{m,mid}(t), \quad \left(\frac{\tau_{end}}{m}\right) \le t < \left(\frac{x - \tau_{end}}{m}\right) \tag{10}$$

$$F_{m,mid}(t) = \begin{bmatrix} f_m\left(L_{m,h}^1(t)\right) & f_m\left(L_{m,h}^2(t)\right) & \cdots & f_m\left(L_{m,h}^k(t)\right) \end{bmatrix}^T \tag{11}$$
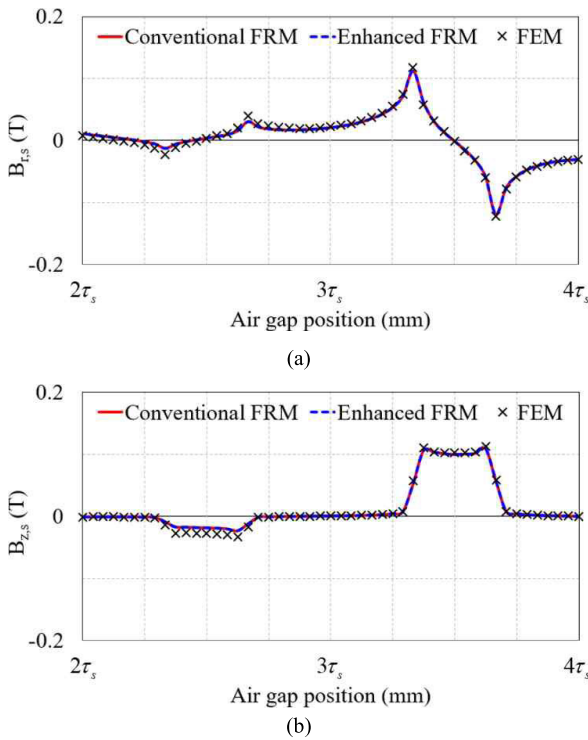
FIGURE 8. Air-gap magnetic flux distribution generated by armature reaction. (a) *r*-component. (b) *z*-component.

where $F_{m,mid}$ is the basis-matrix of the mover, P is the number of poles, m is the velocity, x is the stoke, f_m is the basis-function of the mover, $L^k_{m,h}$ is the reference magnetic flux distribution at kth position in air-gap. The basis-function of the mover requires a FE analysis when the armature winding is not excited and the PM is included. As shown in Fig. 6, due to the back-iron in the stator, the longitudinal end effects occur at both ends of the PM.

B_m can be presented as the linear sum of the air-gap magnetic flux distribution produced by the individual PMs. $F_{m,mid}$ is reconstructed according to the mover position by the basis-function, and the sweeping of the basis-function is expressed as follows:

$$L^i_m(t) = L^{i+\gamma\tau_s}_m(t + \gamma\tau_s/m) \quad (12)$$

$$\gamma = 0, 1, 2, \ldots, (l/\tau_s - 1) \quad (13)$$

where γ is the sweeping coefficient of the mover, l is the air-gap length. $F_{m,mid}$ is repeated every slot pitch and the sweeping can be possible in $\tau_{end}/m \leq t < (x\text{-}\tau_{end})/m$. After the sweep, since the air-gap of the LTPMM is finite, it is necessary to shift the position of the air-gap flux distribution corresponding to the mover movement. The sweeping and shifting are performed simultaneously in (12)-(13).

However, in Fig. 6 (a) and (c), when the mover reaches the end of the stator and the distance between the end of PM and stator is less than τ_{end}, the air-gap flux distribution is no longer predictable. Therefore, the additional basis-matrix of the mover is needed as follows:

$$B_m(t) = F_{m,end}(t)$$
$$0 \leq t < \left(\frac{\tau_{end}}{m}\right), \quad \left(\frac{x - \tau_{end}}{m}\right) \leq t < \left(\frac{x}{m}\right) \quad (14)$$
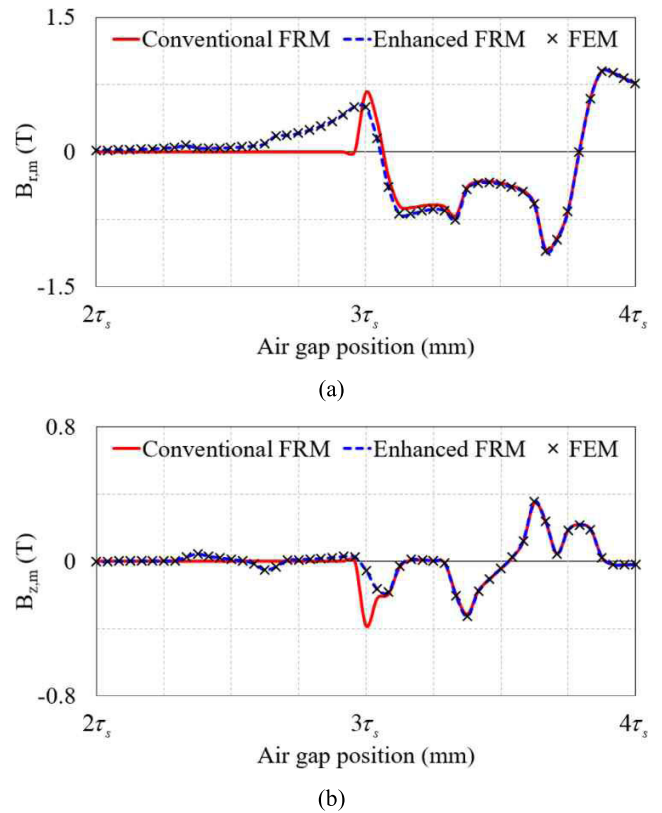

FIGURE 9. Air-gap magnetic flux distribution generated by PM. (a) *r*-component. (b) *z*-component.

where $F_{m,end}$ is the basis-matrix when the end of the PM is located within τ_{end} from the end of the stator.

Fig. 9 shows comparison results. In the results of the conventional FRM, the reference magnetic flux distribution is obtained when the mover is located at the initial time. The difference between the waveforms will cause a large error because it will be repeated several times for each position of the mover by the basis-function.

In Fig. 10, the flowchart of the proposed FRM is presented. At the initial time, the mover is fully retracted to the left end of the LTPMM. First, the static FE analysis is performed to obtain a reference magnetic flux distribution for the basis-function of mover and stator. Then, in Fig. 10, it follows the blue path until the end of the PM is τ_{end} away from the end of the stator. When the PM is located more than τ_{end} from the end of the stator, the FRM flows along the red path. This flow is repeated until the mover enters the other end of the LTPMM. Finally, the thrust of the LTPMM is calculated using B_m and B_s reconstructed from each basis-function.

V. FORCE CALCULATION

The force is calculated using the Maxwell stress tensor (MST) as follows:

$$F = \int_S \overset{\leftrightarrow}{T} \cdot \hat{n}\, dS \quad (15)$$

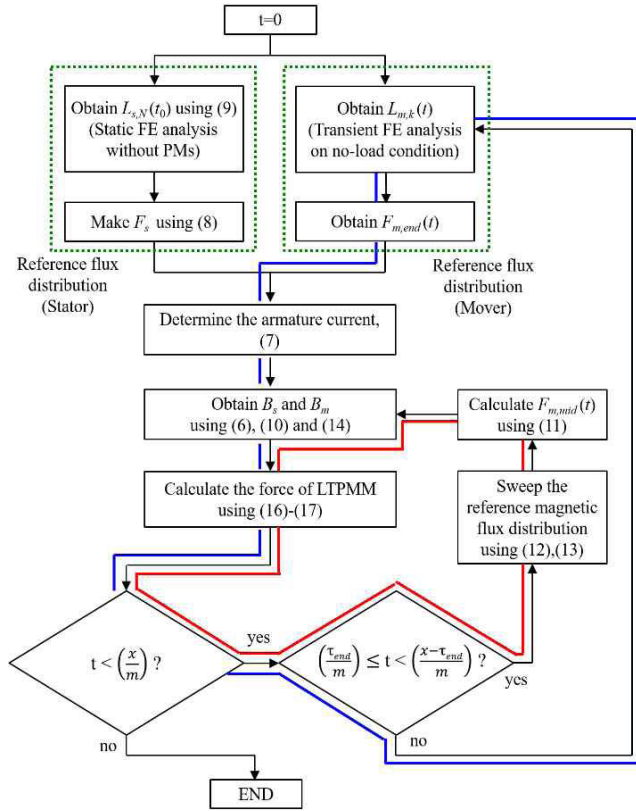where S is the surface area in middle of the air-gap, $\hat{n}$ is the normal vector of the S and $\overset{\leftrightarrow}{T}$ is the MST. For the 3-D

FIGURE 10. Flowchart of the enhanced FRM.

FIGURE 11. Cross section of the LTPMM.

FIGURE 12. Detent force.

cylindrical coordinate system, $\overset{\leftrightarrow}{T}$ is

$$
\overset{\leftrightarrow}{T} = \begin{bmatrix} T_{rr} & T_{r\theta} & T_{rz} \\ T_{\theta r} & T_{\theta\theta} & T_{\theta z} \\ T_{zr} & T_{z\theta} & T_{zz} \end{bmatrix}
$$

$$
= \begin{bmatrix} \dfrac{B_r^2 - B_\theta^2 - B_z^2}{2\mu_0} & \dfrac{B_r B_\theta}{\mu_0} & \dfrac{B_r B_z}{\mu_0} \\ \dfrac{B_r B_\theta}{\mu_0} & \dfrac{B_\theta^2 - B_r^2 - B_z^2}{2\mu_0} & \dfrac{B_\theta B_z}{\mu_0} \\ \dfrac{B_r B_z}{\mu_0} & \dfrac{B_\theta B_z}{\mu_0} & \dfrac{B_z^2 - B_r^2 - B_\theta^2}{2\mu_0} \end{bmatrix}
$$

(16)

assuming $B_\theta = 0$ to analyze an axisymmetric model, $\overset{\leftrightarrow}{T}$ can be simplified as follows:

$$
\overset{\leftrightarrow}{T} = \begin{bmatrix} \dfrac{B_r^2 - B_z^2}{2\mu_0} & \dfrac{B_r B_z}{\mu_0} \\ \dfrac{B_r B_z}{\mu_0} & \dfrac{B_z^2 - B_r^2}{2\mu_0} \end{bmatrix}
$$

(17)

In the LTPMM, the force is classified into the normal force and end force [25]. The normal force is related to the relationship between the stator teeth and the magnet. The end force is generated by the magnetic flux density at the end section of the stator.

Fig. 11 shows the cross section of the LTPMM. In Fig. 11, the $\hat{n}$ of the normal force and end force are $+r$ and $\pm z$ respectively. Using (15) and (17), the thrust force of the
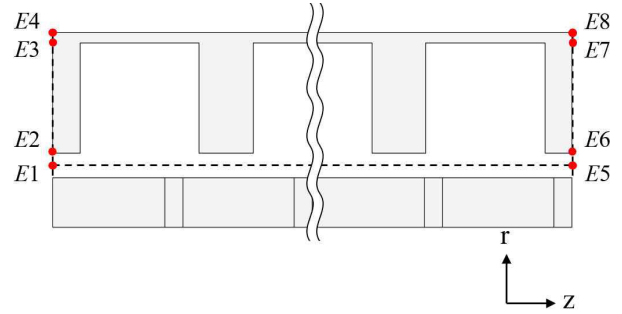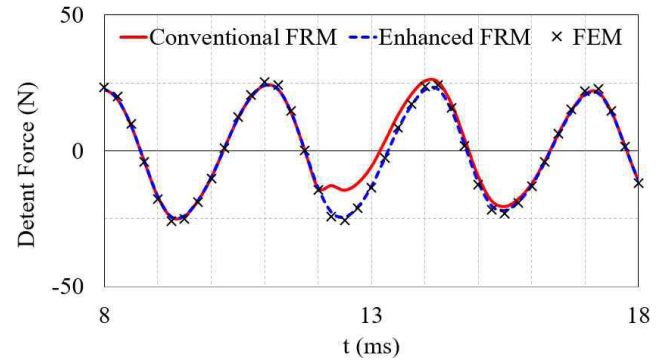
LTPMM can be calculated as (18).

$$
F_z = F_{z,normal} + F_{z,left\_end} + F_{z,right\_end} \tag{18}
$$

$$
F_{z,normal} = \frac{1}{\mu_0} \oint \int_{E1E5} B_r B_z \, d\theta dz \tag{19}
$$

$$
F_{z,left\_end} = \frac{1}{2\mu_0} \oint \int_{E1E2} \left(B_r^2 - B_z^2 \right) d\theta dr
$$
$$
+ \frac{1}{2\mu_0} \oint \int_{E2E3} \left(B_r^2 - B_z^2 \right) d\theta dr
$$
$$
+ \frac{1}{2\mu_0} \oint \int_{E3E4} \left(B_r^2 - B_z^2 \right) d\theta dr \tag{20}
$$

$$
F_{z,right\_end} = \frac{1}{2\mu_0} \oint \int_{E5E6} \left(B_r^2 - B_z^2 \right) d\theta dr
$$
$$
+ \frac{1}{2\mu_0} \oint \int_{E6E7} \left(B_r^2 - B_z^2 \right) d\theta dr
$$
$$
+ \frac{1}{2\mu_0} \oint \int_{E7E8} \left(B_r^2 - B_z^2 \right) d\theta dr \tag{21}
$$

where E1 to E8 are positions at both ends of the stator back-iron to distinguish the influence of the leakage flux.

VI. RESULT

Under no-load conditions, the total air-gap magnetic flux density includes only the B_m produced by the PMs. Therefore, the detent force calculation of the LTPMM can be performed using the basis-function of the mover. In Fig. 12, the detent force of the FRM and FEM are compared. It is noted that the basic-function of the conventional FRM provides the error of the reconstructed field by sweeping the distorted field at the end of the stator. Compared with the results of the FEM, it can
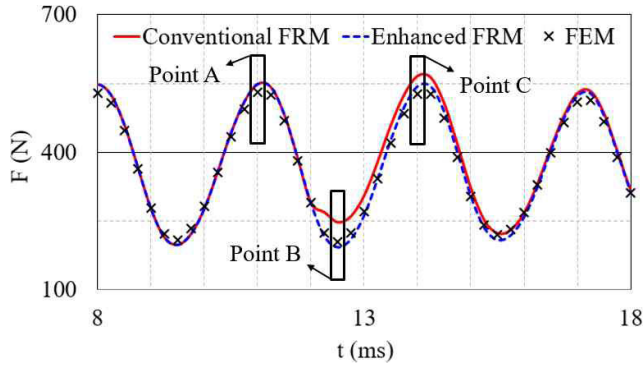
FIGURE 13. Thrust force.

be seen that the error of the enhanced FRM is less than 5%, while the error of the conventional FRM is up to 21.2%.

On the other hand, for the calculation of thrust, both the basic-functions of mover and stator are used. First, the reference magnetic flux distribution for sweeping of each basis-function is obtained using FE static analysis. The basis-matrix is calculated in (8) and (11), and the thrust is calculated in (18) using the reconstructed entire field.

Fig. 13 illustrates comparison results of the thrust force in LTPMM. In Fig. 13, the Point A is when the mover is positioned at the end of the stator, and Point B and C are when the mover is more than τ_{end} from the end of the stator.

Since the basis-function of the conventional FRM selects the reference magnetic flux distribution when the mover is located at the initial time, at Point A, the error between the FRMs and the FEM is 3.45%. At the Point B, the difference between the conventional FRM and FEM was 21.1%, while the difference between the enhanced FRM and FEM was 5.5%.

The Fig. 14 shows the distribution of the magnetic flux density inside the back-iron of the stator. Four cases were adopted to verify the feasibility of the FRM according to the saturation effect. The measurements of the B were performed on the same element of each case. In Table 2, the results of the FRM and FE analysis are compared. For Case 1, 2 and Case 3, the results are under soft magnetic saturations and the resulting difference between the FE analysis and FRM is less than 1.8%. In Case 5, 6 and Case 7, the difference is still acceptable at less than 7.4%, even under hard saturation conditions.

Under the same simulation conditions (CPU Intel core i7-6700K 4.00GHz, RAM 16GB), for 3-D model, the FE analysis required 38h 2m, while the FRM took 4h 13m. The model has 270 105 elements, and the simulation was performed for full stroke of the LTPMM. The FRM provides an 88.9% reduction in time costs compared to FE analysis. During the optimization process, the computational time difference between these two methods becomes larger in situations where the dimensions of the model should change. Given that the mover and stator fields are independent of each other in the FRM, this is advantageous for analyzing the characteristics of pole and coil combinations. If various magnet
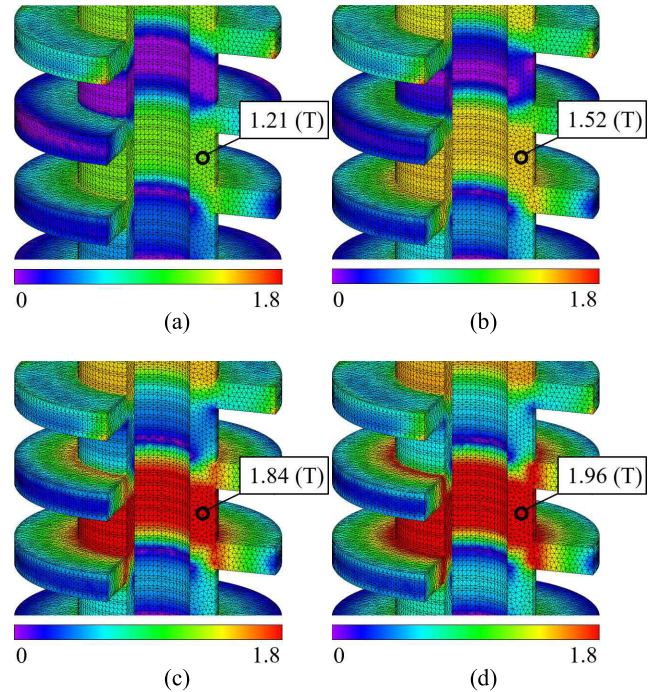

FIGURE 14. Magnetic flux density distribution in stator. (a) Case 1. (b) Case 3. (c) Case 5. (d) Case 7.

TABLE 2. Comparison results.

Case	B_{max}(T)	$F_{z,min}$(N)			$F_{z,avg}$(N)			$F_{z,max}$(N)		
		FEM	FRM	error	FEM	FRM	error	FEM	FRM	error
1	1.21	884	887	0.3%	1109	1118	0.8%	1365	1367	0.2%
2	1.32	996	1006	1.0%	1232	1239	0.6%	1488	1493	0.3%
3	1.52	1159	1180	1.8%	1417	1419	0.1%	1670	1678	0.5%
4	1.63	1317	1347	2.2%	1591	1602	0.7%	1841	1866	1.4%
5	1.84	1520	1569	3.2%	1805	1848	2.4%	2039	2116	3.8%
6	1.86	1615	1680	4.0%	1902	1971	3.7%	2125	2241	5.5%
7	1.96	1707	1791	4.9%	1991	2094	5.2%	2203	2367	7.4%

TABLE 3. Test condition.

Mover speed (m/s)	2
Current (A)	9
Voltage (V)	95
Stroke (mm)	144

shapes should be reflected in a specific coil structure, there is no need for additional armature reaction field analysis, and when considering changes in the winding configuration in a specific magnet shape, additional FE calculations to obtain the no-load field are not required. In addition, when analyzing with changes in excitation current, the FE analysis should be recalculated, whereas in the case of the FRM, it is possible to predict the result with acceptable accuracy by using the basis function.

VII. EXPERIMENTAL VERIFICATION

To validate the enhanced FRM, prototype LTPMM presented in this paper has been manufactured and tested. The specification of the prototype LTPMM is listed in Table 1. The outer diameter and overall length were determined taking into account the space occupied by the suspension in the vehicle. Table 3 shows the test condition. The test setup is
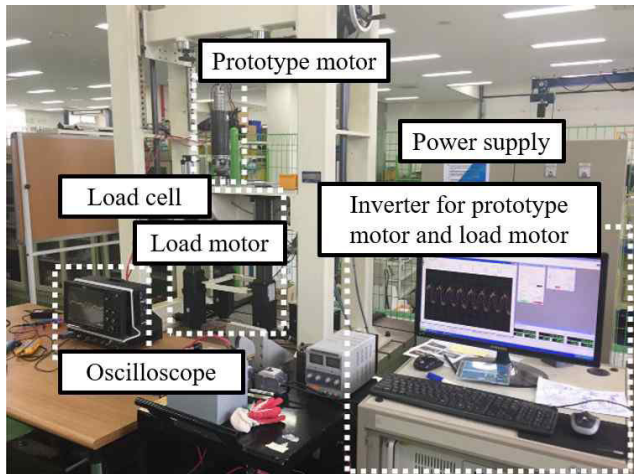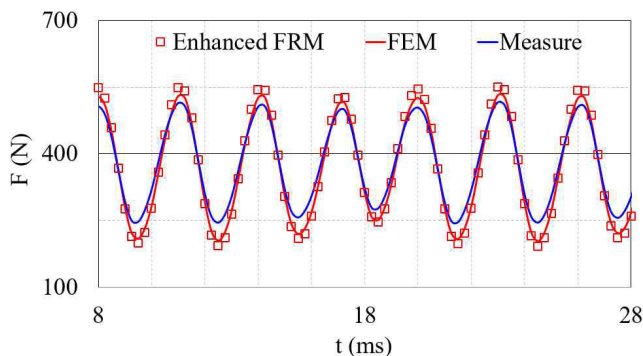
FIGURE 15. Test setup.

FIGURE 16. Experimental results.

shown in Fig. 15. For measuring thrust, the specially designed load cell was attached on the housing. Four load-motors actuate the prototype motor. The speed and thrust load are controlled by inverter for load motors and the thrust force is generated by inverter for prototype motor. The comparison of calculated and measured thrust characteristics is shown in Fig. 16. The difference between the enhanced FRM and experimental result was 3.7% on average.

VIII. CONCLUSION

The contribution of this paper is to present a method for fast evaluation of the force calculation and magnetic flux distribution of linear motors using the FRM. This paper considers the LTPMM for the electromagnetic active suspension of vehicles. We adopted FRM to reduce computational burden for modeling LTPMM. Since the road condition changes every moment, detailed operation is necessary for the comfort of the driver. For this reason, accurate thrust force calculations are an important factor in modeling the LTPMM. However, because the LTPMM has short mover and short stator, the longitudinal end effect is significant. The r- and z-components of the air-gap flux were analyzed to investigate the longitudinal end effect. Finally, we proposed an enhanced FRM taking consideration into this end effect of the LTPMM. We found that using the proposed FRM compared to the FE analysis resulted in a 88.9% reduction in time cost. Furthermore, It can

be used not only for the LTPMM, but also for exterior/interior magnet type, radial/axial/halbach magnetization patterns, and even flat-type linear motors.

REFERENCES

[1] C. Marina Martinez, M. Heucke, F.-Y. Wang, B. Gao, and D. Cao, "Driving style recognition for intelligent vehicle control and advanced driver assistance: A survey," *IEEE Trans. Intell. Transp. Syst.*, vol. 19, no. 3, pp. 666–676, Mar. 2018.

[2] H. Chu, L. Guo, B. Gao, H. Chen, N. Bian, and J. Zhou, "Predictive cruise control using high-definition map and real vehicle implementation," *IEEE Trans. Veh. Technol.*, vol. 67, no. 12, pp. 11377–11389, Dec. 2018.

[3] B. L. J. Gysen, J. J. H. Paulides, J. L. G. Janssen, and E. A. Lomonova, "Active electromagnetic suspension system for improved vehicle dynamics," *IEEE Trans. Veh. Technol.*, vol. 59, no. 3, pp. 1156–1163, Mar. 2010.

[4] W. Sun, Q. Li, L. Sun, L. Zhu, and L. Li, "Electromagnetic analysis on novel rotor-segmented axial-field SRM based on dynamic magnetic equivalent circuit," *IEEE Trans. Magn.*, vol. 55, no. 6, Jun. 2019, Art. no. 8103105.

[5] M. M. Kiani, W. Wang, and W.-J. Lee, "Elimination of system-induced torque pulsations in doubly-fed induction generators via field reconstruction method," *IEEE Trans. Energy Convers.*, vol. 30, no. 3, pp. 1228–1236, Sep. 2015.

[6] H.-J. Park, H.-K. Jung, S.-Y. Jung, Y.-H. Chae, and D.-K. Woo, "Field reconstruction method in axial flux permanent magnet motor with overhang structure," *IEEE Trans. Magn.*, vol. 53, no. 6, Jun. 2017, Art. no. 8201304.

[7] E. Ajily, M. Ardebili, and K. Abbaszadeh, "Magnet defect and rotor eccentricity modeling in axial-flux permanent-magnet machines via 3-D field reconstruction method," *IEEE Trans. Energy Convers.*, vol. 31, no. 2, pp. 486–495, Jun. 2016.

[8] E. Ajily, K. Abbaszadeh, and M. Ardebili, "Three-dimensional field reconstruction method for modeling axial flux permanent magnet machines," *IEEE Trans. Energy Convers.*, vol. 30, no. 1, pp. 199–207, Mar. 2015.

[9] C. Lin, W. Wang, M. McDonough, and B. Fahimi, "An extended field reconstruction method for modeling of switched reluctance machines," *IEEE Trans. Magn.*, vol. 48, no. 2, pp. 1051–1054, Feb. 2012.

[10] D. Torregrossa, B. Fahimi, F. Peyraut, and A. Miraoui, "Fast computation of electromagnetic vibrations in electrical machines via field reconstruction method and knowledge of mechanical impulse response," *IEEE Trans. Ind. Electron.*, vol. 59, no. 2, pp. 839–847, Feb. 2012.

[11] D. Torregrossa, A. Khoobroo, and B. Fahimi, "Prediction of acoustic noise and torque pulsation in PM synchronous machines with static eccentricity and partial demagnetization using field reconstruction method," *IEEE Trans. Ind. Electron.*, vol. 59, no. 2, pp. 934–944, Feb. 2012.

[12] A. Khoobroo and B. Fahimi, "Magnetic flux estimation in a permanent magnet synchronous machine using field reconstruction method," *IEEE Trans. Energy Convers.*, vol. 26, no. 3, pp. 757–765, Sep. 2011.

[13] B. J. Deken and S. D. Pekarek, "Enhanced field reconstruction method for the efficient analysis of permanent magnet synchronous machines," *IEEE Trans. Energy Convers.*, vol. 27, no. 3, pp. 661–669, Sep. 2012.

[14] D. Wu, S. D. Pekarek, and B. Fahimi, "A voltage-input-based field reconstruction technique for efficient modeling of the fields and forces within induction machines," *IEEE Trans. Ind. Electron.*, vol. 57, no. 3, pp. 994–1001, Mar. 2010.

[15] W. Wang, M. Kiani, and B. Fahimi, "Optimal design of doubly fed induction generators using field reconstruction method," *IEEE Trans. Magn.*, vol. 46, no. 8, pp. 3453–3456, Aug. 2010.

[16] S. G. Min and B. Sarlioglu, "3-D performance analysis and multiobjective optimization of coreless-type PM linear synchronous motors," *IEEE Trans. Ind. Electron.*, vol. 65, no. 2, pp. 1855–1864, Feb. 2018.

[17] S. E. Abdollahi, M. Mirzayee, and M. Mirsalim, "Design and analysis of a double-sided linear induction motor for transportation," *IEEE Trans. Magn.*, vol. 51, no. 7, Jul. 2015, Art. no. 8106307.

[18] A. Boduroglu, M. Gulec, Y. Demir, E. Yolacan, and M. Aydin, "A new asymmetric planar V-shaped magnet arrangement for a linear PM synchronous motor," *IEEE Trans. Magn.*, vol. 55, no. 7, Jul. 2019, Art. no. 8105905.

[19] K.-H. Shin, H.-I. Park, J.-M. Kim, H.-W. Cho, and J.-Y. Choi, "Optimum iron pole design of a tubular linear synchronous machine with double-sided axially magnetized permanent magnets considering leakage flux," *IEEE Trans. Magn.*, vol. 52, no. 7, Jul. 2016, Art. no. 8203604.

[20] B. Gysen, K. J. Meessen, J. Paulides, and E. A. Lomonova, "Semi-analytical calculation of the armature reaction in slotted tubular permanent magnet actuators," *IEEE Trans. Magn.*, vol. 44, no. 11, pp. 3213–3216, Nov. 2008.

[21] Z. Jiao, T. Wang, and L. Yan, "Design of a tubular linear oscillating motor with a novel compound Halbach magnet array," *IEEE/ASME Trans. Mechatronics*, vol. 22, no. 1, pp. 498–508, Feb. 2017.

[22] Z. Q. Zhu, Z. P. Xia, and D. Howe, "Comparison of Halbach magnetized brushless machines based on discrete magnet segments or a single ring magnet," *IEEE Trans. Magn.*, vol. 38, no. 5, pp. 2997–2999, Sep. 2002.

[23] W. Zhu, B. Fahimi, and S. Pekarek, "A field reconstruction method for optimal excitation of permanent magnet synchronous machines," *IEEE Trans. Energy Convers.*, vol. 21, no. 2, pp. 305–313, Jun. 2006.

[24] D. Wu, S. D. Pekarek, and B. Fahimi, "A field reconstruction technique for efficient modeling of the fields and forces within induction machines," *IEEE Trans. Energy Convers.*, vol. 24, no. 2, pp. 366–374, Feb. 2009.

[25] C. Liu, H. Yu, M. Hu, Q. Liu, and S. Zhou, "Detent force reduction in permanent magnet tubular linear generator for direct-driver wave energy conversion," *IEEE Trans. Magn.*, vol. 49, no. 5, pp. 1913–1916, May 2013.

KI-HOON KIM (Student Member, IEEE) received the B.S. degree in electrical engineering from Yeungnam University, Gyengbuk, South Korea, in 2017, where he is currently pursuing the Ph.D. degree.

His current research interests include numerical analysis and design of electrical machines.

DONG-KYUN WOO received the B.S. degree in electrical engineering from Yonsei University, Seoul, South Korea, in 2007, and the Ph.D. degree from Seoul National University, Seoul, in 2014.

He has conducted research with the Power and Industrial Systems Research and Development Center, Hyosung, from 2014 to 2015. He is currently a Professor with the School of Electrical Engineering, Yeungnam University, Gyengbuk, South Korea. His research interests include numerical analysis and design of electric machines.

● ● ●